A Micro EIT Sensor for Real-time and Non-destructive 3-D Cultivated Cell Imaging

A Micro EIT Sensor for Real-time and Non-destructive 3-D Cultivated Cell Imaging

Xipeng Yin, Hancong Wu, *Student Member*, Jiabin Jia, *Member, IEEE*, Yunjie Yang*, *Member, IEEE*

***Abstract*—A micro EIT sensor with radially distributed planar electrodes was designed, characterized and experimentally validated for real-time and non-destructive 3-D cultivated cell imaging. The 12-mm cylindrical sensor was consisted of 17 circular micro electrodes, including 16 sensing electrodes and a reference electrode. The sensor's characteristics, i.e. dynamic range of measurement and sensitivity, was examined by finite element simulations and actual measurements. MCF-7 breast cancer cells were then cultivated to form the spherical aggregate and 3-D image reconstructions were performed on three solutions containing varying number and locations of cell aggregates. Furthermore, real-time imaging of cell-drug response between a MCF-7 cell aggregate and diluted Triton X-100 solution was carried out and the 3-D conductivity variation associated with this transient process was captured successfully and reconstructed in high accuracy. The simulation, 3-D cell aggregate imaging experiments and real-time reconstructions of cell-drug response suggest that the EIT based micro sensor has the potential to study non-destructively and in real time the dynamic biological behavior of a 3-D cell culture system.**

***Index Terms*—3-D cell imaging, Electrical Impedance Tomography, image reconstruction, micro sensor.**

I. Introduction

EMERGING in the early 1980's [1], Electrical Impedance Tomography (EIT) is one of the electrical tomographic imaging modalities to visualize non-intrusively the absolute value or variation of electrical conductivity within a region of interest [2-4]. The principle of EIT is to apply successively an electrical current on the selected electrodes and measure the induced voltages on the other electrode pairs. Current excitation and voltage acquisition are repeated continuously and rapidly until all the non-redundant electrode combinations are deployed. A completed set of data can then produce one frame of a sliced 2-D or a 3-D image based on certain *a priori* knowledge to estimate the spatial distribution of conductivity.

Attributing to the ability of high-speed, non-radiation, and non-intrusive sensing, in recent years EIT has been exploited extensively in industrial process imaging, in order to estimate critical process parameters and capture transient phenomena. Relevant cases include the use of EIT for real-time multiphase flow characterization [5], sedimentation monitoring [6], liquid mixing dynamics investigation [7], spatial damage in concrete imaging [8], and pressure-sensitive artificial skin of robotics [9]. Beyond the high maturity of industrial practice, EIT has also aroused enormous interest in biomedical research, aiming at monitoring and assessing the transient biological behaviors in real time. Reported research includes the use of EIT for fast neural activity imaging [10], breast cancer imaging [11], lung ventilation imaging [12] and cell sedimentation imaging [13], etc.

This work probed an emerging biomedical application of EIT in 3-D cultivated cell imaging to study non-destructively and in real time the dynamic biological behavior of a 3-D cell culture system. Cell culture commonly exists in many biomedical research and industries, such as tissue engineering, pharmaceutical industry and cancer research [14]. Two typical cell culture formats, i.e. 2-D cell culture [15] and 3-D cell culture [16], are illustrated in Fig. 1. Compared to the traditional 2-D cell culture, which cultivates monolayer cells on flat and rigid substrates, cell culture using a 3D model facilitates the behavior which is closer to the real complex *in vivo* conditions as well as the delivery of research outcomes to *in vivo* applications [16].

In various cell culturing processes, non-intrusive sensing technique with high temporal resolution is requisite to monitor either transient or secular cellular activities, such as cell-drug response and bone tissue regeneration, etc. For a biological process based on 2-D cultivated cells, optics based methods such as microscopy [17], and electrical based methods such as Electrical Impedance Spectroscopy (EIS) [18] can be applied easily to monitor the process. However, for a dynamic biological process based on 3-D cultivated cells, few techniques have been verified effective and maturely applied in real-time and non-destructive monitoring. The fluorescence staining methods are possible to be used in 3-D cell assay, but it suffers from the non-uniform diffusion of the fluorescence dyes in the thick cell aggregates, which leads to inaccurate results [19]. Tyrpan blue assay under microscope can be employed in 3-D cell counting [20], but this method is destructive and the samples under test cannot be used in the future experiments. Indirect methods such as MTT assay are currently applied in 3-D cell analysis [21], but such techniques require additional processing and cannot be applied to high throughput screening. Sensing techniques capable of performing 3-D, real-time and non-destructive imaging for 3-D cultivated cells are still under track.

Manuscript received xx, xx, 2018. This work was supported in part by the scholarship from China Scholarship Council (CSC) under the Grant CSC No. 01606295050 and the 2015 IEEE I&M Society Graduate Fellowship Award.

Xipeng Yin is with the School of Electronics and Information, Northwestern Polytechnical University, Xi'an, China.

Hancong Wu, Jiabin Jia and Yunjie Yang are with the Agile Tomography Group, Institute for Digital Communications, School of Engineering, The University of Edinburgh, Edinburgh, EH9 3JL, UK (*Corresponding author, e-mail: y.yang@ed.ac.uk)

Note that Xipeng Yin and Hancong Wu contribute equally to this work.

To bridge this gap, in this work we propose a micro EIT sensor with radially distributed planar electrodes for real-time and non-destructive 3-D cultivated cell imaging. The design and manufacture of sensor was demonstrated and the 3-D image reconstruction based on Basis Pursuit Denoising (BPDN) approach with median filter was introduced. The sensor was characterized based on simulation and experiment data in terms of measurement data and sensitivity. 3-D image reconstruction on MCF-7 human breast cancer cell aggregates was performed. Beyond that, real-time 3-D imaging of cell-drug response between MCF-7 cell aggregate and Triton X-100 was achieved based on the proposed techniques.

This work demonstrates proof-of-principle that micro EIT sensor based on planar electrode configuration is well suited for multicellular spheroids imaging, which represents a non-destructive cell viability assay based on membrane integrity. Taken together with EIT spatial resolution, the innovative approaches developed in the work will enable non-destructive, real-time monitoring of the cellular dynamics within a 3-D cell culture system, e.g. cell-drug response across all layers of cell spheroids. This is deemed a critical challenge and cannot be realized by other imaging modalities to the date.

II. Sensor Design and 3-D Image Reconstruction

A. Theory of EIT

EIT estimates the conductivity inside a computational domain, i.e. $\Omega \subset \mathbb{R}^q$ where $q = 2, 3$, as spatially distributed parameters by injecting currents through boundary electrodes and measuring the corresponding differential voltages across other electrode pairs [3]. The electromagnetic field induced by the injected current is governed by Maxwell's equations. By assuming low frequencies and small field strengths, the measurements can be modelled by the Complete Electrode Model (CEM) [22, 23], i.e.

$$\nabla \cdot \big(\sigma(x,y)\nabla u(x,y)\big) = 0, \ \ (x,y) \in \Omega \tag{1}$$

$$u + z_\ell \sigma \frac{\partial u}{\partial n} = U_\ell, \ (x,y) \in e_\ell, \ \ell = 1, \dots, \mathcal{L} \tag{2}$$

$$\int_{e_\ell} \sigma \frac{\partial u}{\partial n} dS = I_\ell, \ \ell = 1, \dots, \mathcal{L} \tag{3}$$

$$\sigma \frac{\partial u}{\partial n} = 0, \ (x,y) \in \partial\Omega \setminus \cup_{\ell=1}^{\mathcal{L}} e_\ell \tag{4}$$

where σ and u denote respectively the conductivity and electric potential inside Ω; $\mathcal{L}$ is the number of electrodes and e_ℓ is the ℓ^{th} electrode; z_ℓ represents the contact impedance of e_ℓ; n is the outward unit norm of the boundary $\partial\Omega$; U_ℓ and I_ℓ represent the electrical potential and injected current on e_ℓ, respectively.

The existence and uniqueness of the solution u are further ensured by the conservation of charges imposed by Eq. (5) and the choice of ground voltage in order to have Eq. (6).

$$\sum_{\ell=1}^{\mathcal{L}} I_\ell = 0 \tag{5}$$

$$\sum_{\ell=1}^{\mathcal{L}} U_\ell = 0 \tag{6}$$

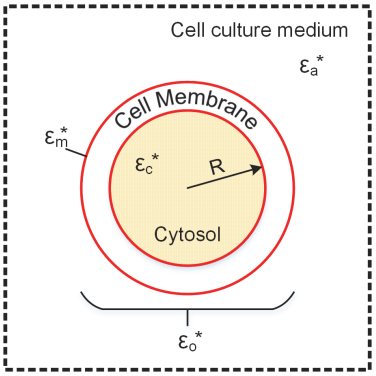

Fig. 1. The single shell model for analytical calculation.

The relation between the conductivity in Ω and the boundary potential measurements is in essence nonlinear. Whilst this nonlinear relation can be linearized by assuming that the conductivity perturbation $\Delta\sigma \in \mathbb{R}^n$ with respect to a reference is small, which can be stated by:

$$\Delta V = J\Delta\sigma \tag{7}$$

where $\Delta V \in \mathbb{R}^m$ is the vector of measured voltage variations attributing to the conductivity perturbation. $J \in \mathbb{R}^{m\times n}$ is the Jacobian (sensitivity matrix), which is calculated based on the reference.

The objective of EIT image reconstruction is to numerically approximate $\Delta\sigma$ based on the voltage measurement ΔV. It is an ill-posed inverse problem and regularization techniques [24, 25] are commonly employed in order to obtain stable solutions.

B. Cell Model and Theoretical Analysis

Several simplified cell models have been proposed [26] to calculate analytically the electrical properties of the complex heterogeneous cells. Most models are based on the assumption that the cell is enclosed by a layer separating its cytoplasm from the external media. In this work, the Maxwell–Wagner–Sillars (MWS) model [26-28] as shown in Fig. 1 was adopted for theoretical analysis. In this model, the cell's cytoplasm is assumed to be a uniform conductive medium. The equivalent homogenous complex permittivity of the cell, i.e. ε_o^*, is formulated as:

$$\varepsilon_o^* = \varepsilon_m^* \frac{2(1-q)\varepsilon_m^* + (1+2q)\varepsilon_c^*}{(2+q)\varepsilon_m^* + (1-q)\varepsilon_c^*} \tag{8}$$

where ε_m^* and ε_c^* denote respectively the complex permittivity of the cell membrane and the cytoplasm, and $q = [R/(R+d_m)]^3$, d_m is the thickness of the membrane. Based on Eq. (8), we can calculate the effective admittance of the cell as:

$$\sigma_o^* = j\omega\varepsilon_0\varepsilon_o^* = \sigma_o + j\omega\varepsilon_0\varepsilon_o \tag{9}$$

where σ_o and ε_o denote respectively the effective conductivity and relative permittivity of the cell and ε_0 represents the

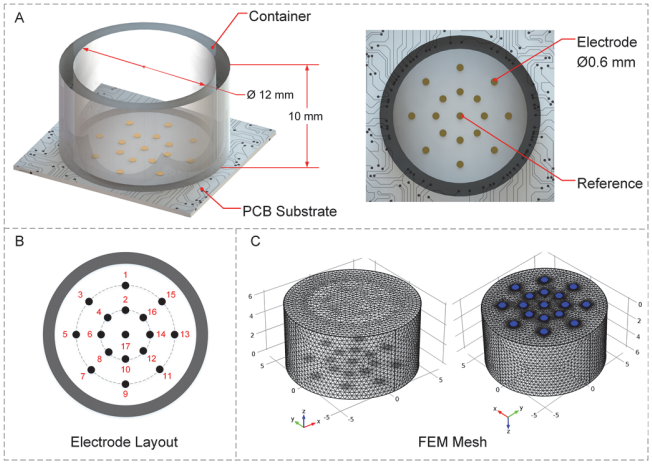

Fig. 2. The designed miniature planar EIT sensor. A: schematic of the sensor. B: electrode layout and index. C: FEM mesh for forward problem calculation (scale in mm).

permittivity of vacuum.

Based on Eq. (9) and the CEM, it is explicit that the local conductivity contrast induced by the cells could be estimated by EIT, and EIT actually reconstructs the equivalent conductivity of the cells. In addition, Eq. (9) also indicates that the electrical properties of the cells are not simple and might depend on frequency. In this study, the selection of current frequency was based on the three dispersion mechanisms (termed α-, β-, and γ-dispersions) introduced by Schwan [29, 30], which characterized the electric properties of biological tissues and cell suspensions. The α-dispersion generally appears below a few kHz and is not easy to measure due to the interference from electrode polarization effects. The β-dispersion ranges from around 10 kHz up to several MHz and is correlated with the interfacial polarization due to the existence of the insulating membrane surrounding the cells. The γ-dispersion is above 10 GHz and is related to the polarization of water molecules. The conductivity changes observed at 10 kHz is associated with the cell membranes integrity (β-dispersion). The dispersion almost disappears after the membrane is disrupted or permeabilized by detergents, such as Triton X-100. This frequency also locates in the optimal region of frequency for Electric Cell substrate Impedance Sensing (ECIS) within which the cells have different electrical properties with the culture medium [31]. Therefore, in this study, we focus on the β-dispersion and the injected current's frequency is set as 10 kHz.

C. Sensor Design

A miniature planar EIT sensor was designed to measure the 3-D conductivity in a 3-D cell culture system. It consists of an array of planar micro electrodes embedded in the surface of a Printed Circuit Board (PCB) substrate. Fig. 2 (a) illustrates the schematic of the designed sensor. The inner diameter of the cylindrical sensing chamber is 12 mm. The height of the chamber is 10 mm. There are 17 circular micro electrodes distributed in the surface of PCB substrate including a reference electrode which can be connected to ground. The diameter of each electrode is 0.6 mm. The index of electrodes are labeled in Fig. 2 (b). Fig. 2 (c) demonstrates the Finite Element Modelling (FEM) mesh applied in this work to calculate forward solutions. The mesh contains 235,000 domain elements and shows the actual volume of regions to be imaged.

D. 3-D Image Reconstruction Method

The objects to be imaged in 3-D cell culture systems usually incur weak conductivity changes in a small scale. The inaccurate estimation of the objects' dimension and numerous artefacts appeared in the reconstructed images make such cases particularly challenging. In this work, a 3-D EIT reconstruction algorithm previously reported by the authors [32] was used to estimate the sparse conductivity distribution of 3-D cell culture systems. The EIT image reconstruction problem is formulated by using the Basis Pursuit Denoising (BPDN) approach [33, 34] in order to seek sparse solutions to the under-determined and ill-posed problem, which is stated by:

$$\begin{cases} min_{\Delta\sigma} & \|\Delta\sigma\|_1 \\ s.t. & \|J\Delta\sigma - \Delta V\|_2^2 \le \epsilon \end{cases} \tag{10}$$

where ϵ is a positive scalar which estimates the noise level of the measurement data.

The spectral projected-gradient based algorithm was applied to solve Eq. (10), which is proved efficient for optimization problems involving large-scale matrices. The detail of implementing the algorithm can be referred to [34]. In this work, for all occasions, we set $\epsilon = 0.05 \times \|\Delta V\|_2$, the maximum iteration numbers to be 500, and the iteration termination condition to be $\left\|\Delta\sigma^{(k+1)} - \Delta\sigma^{(k)}\right\|_2 < 10^{-5}$.

Fig. 3 presents the coarse mesh applied in the inversion problem. The sensing domain was discretized into 32×32 voxels horizontally and 20 layers vertically. As a result, the cylindrical domain is consisted of 16240 voxels and, classified by vertical layers, we have

$$\Delta\sigma = \{\Delta\sigma_{h1};\ \Delta\sigma_{h2};\ \ldots;\ \Delta\sigma_{h20}\} \tag{11}$$

where $\Delta\sigma_{hi} \in \mathbb{R}^{812}, i = 1, \ldots, 20$ is a vector containing the conductivity in the i^{th} layer along the vertical direction.

According to our previous work in [32], spike type artefacts commonly exist in the solutions of (10), because planar

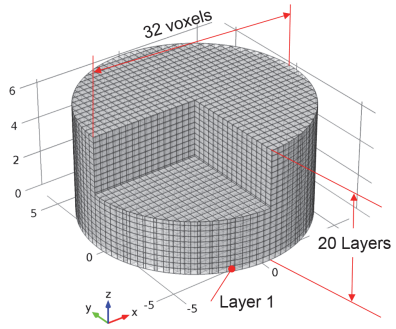

Fig. 3. The coarse mesh for inversion calculation.

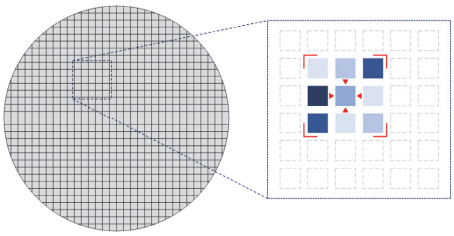

Fig. 4. The median filter applied to a voxel in one layer.

electrode configuration exhibits much higher sensitivity in the layers near the electrode surface and, the contact of imaging objects with the electrodes can also lead to large amplitudes in certain measurements. In order to eliminate the background noise peaks and preserve the edge of the objects, a median filtering operation is performed on each layer of the solution, which is formulated as:

$$\widehat{\Delta\sigma} = \{median(\Delta\sigma_{h1});\ median(\Delta\sigma_{h2}); \dots;\ median(\Delta\sigma_{h20})\} \quad (12)$$

where $\widehat{\Delta\sigma} \in \mathbb{R}^n$ is the final estimated conductivity. $median$ denotes the median filter operator as illustrated in Fig. 4. The median filter utilizes an $m \times m$ sliding window and, in consideration of symmetry, m is usually an odd number [35]. The sliding window mechanism sorts the neighborhood values from small to larger values and replaces the original voxel value with the median value of the sorted neighborhood window. In this work, a 5×5 filter window was applied.

E. Image Quality Assessment

In order to perform quantitative assessment of the image quality, two criteria were employed, i.e. position error and correlation coefficient. The position error is defined by:

$$P_{err} = \|P_{est} - P_{true}\| \quad (13)$$

where P_{est} denotes the geometrical center of the reconstructed objects, which is calculated by finding the local maximum conductivity change. P_{true} denotes the ground truth of the geometrical center of the objects. The position error evaluates the accuracy of estimate the conductivity change center in terms of Euclidean distance.

The correlation coefficient is defined by:

$$C_{corr} = \frac{\sum_{i=1}^{n}(\widehat{\Delta\sigma}_i - \overline{\widehat{\Delta\sigma}})(\Delta\sigma_i - \overline{\Delta\sigma})}{\sqrt{\sum_{i=1}^{n}(\widehat{\Delta\sigma}_i - \overline{\widehat{\Delta\sigma}})^2 \sum_{i=1}^{n}(\Delta\sigma_i - \overline{\Delta\sigma})^2}} \quad (14)$$

where $\Delta\sigma_i$ and $\widehat{\Delta\sigma}_i, i = 1, \dots, n$ denote respectively the i^{th} element of the true conductivity and estimated conductivity. $\overline{\widehat{\Delta\sigma}}$ and $\overline{\Delta\sigma}, i = 1, \dots, n$ denote respectively the mean of the estimated conductivity and true conductivity. Correlation coefficient evaluates the degree to which the distribution of estimated conductivity and ground truth are associated.

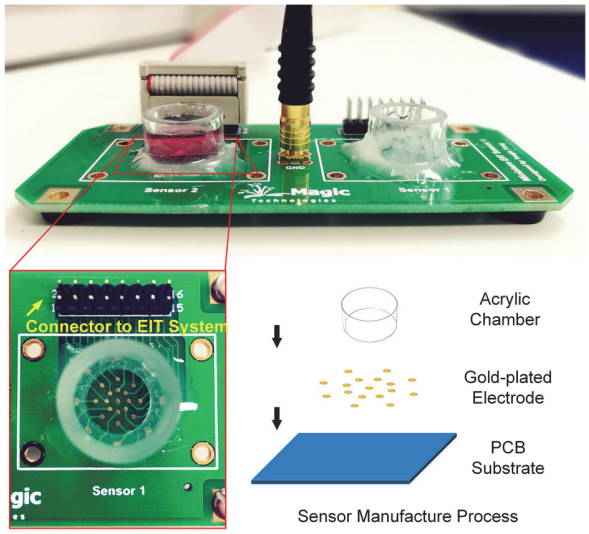

Fig. 5. The manufactured sensor.

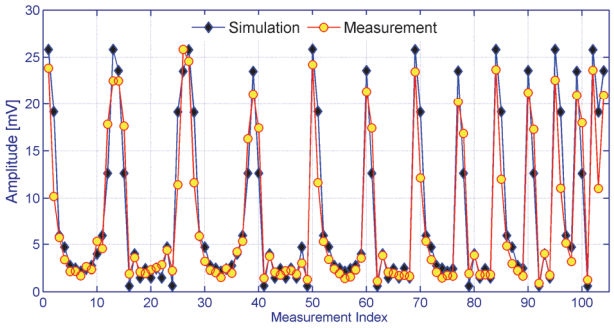

Fig. 6. Measured voltage data vs. simulated voltage data.

III. Sensor Fabrication and Characterization

A. Sensor Fabrication

Fig. 5 shows the manufactured sensor. Two identical sensing chambers were constructed on a PCB substrate in order to provide simultaneous imaging ability for multiple cell culture systems. The micro electrodes were constructed with gilded surfaces in order to improve corrosion resistance. Acrylic tubes were cut precisely to fit on the substrate in order to form two sensing chambers. The sensor interfaces the EIT system with two ribbon cables.

B. Sensor Characterization

The sensor was characterized in terms of measurement data and spatial sensitivity. The voltage data was measured based on adjacent sensing strategy [36]. Fig. 6 shows the comparison of the measured voltage data and the simulated voltage data, which indicates a good correlation. Dynamic range of the measured voltage vector was used to evaluate the requirements of the sensor on impedance measurement electronics, which is defined by:

$$D = \frac{V_{max}}{V_{min}} \quad (15)$$

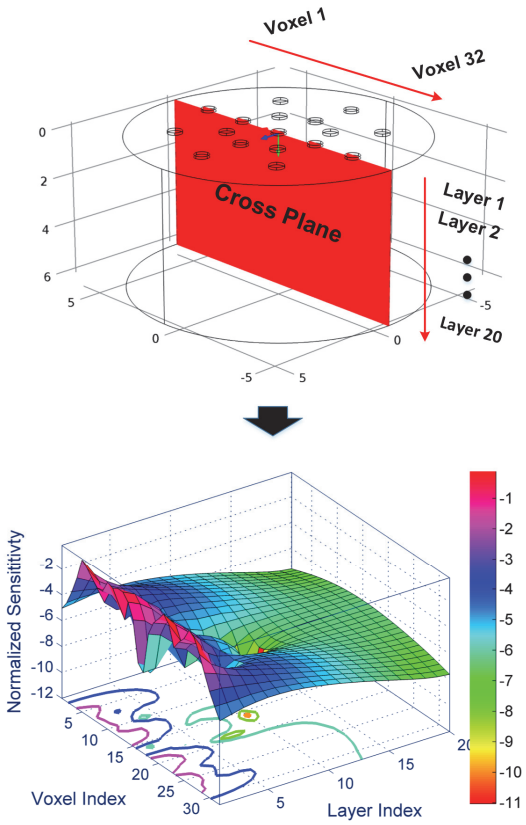

Fig. 7. Logarithmic sensitivity of the sensor at the vertical cross section passing electrode 5, 6, 17, 14, 13.

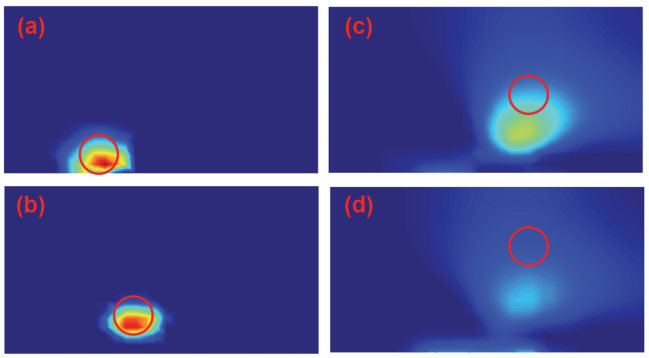

Fig. 8. Reconstructions of simulated spheroids at four different positions of the vertical cross plane shown in Fig. 7. (a) Center of spheroid: voxel index 8, layer index 2. (b) Center of spheroid: voxel index 13, layer index 6. (c) Center of spheroid: voxel index 21, layer index 10. (d) Center of spheroid: voxel index 21, layer index 13.

where V_{max} and V_{min} represent respectively the maximum and minimum value of the voltage vector. Generally, a smaller D is desired as it is easier to be realized in hardware design and better signal to noise ratio can be obtained. Based on simulation results in Fig. 6, the theoretical dynamic range of the sensor is calculated to be 42.40. According to experimental data in Fig. 6, this value is measured to be 34.17 because of the imperfection of the manufacture. The results suggest that the dynamic range is located in a reasonable range, which can be handled by a typical EIT system.

Sensitivity is a critical indicator for identifying the effective sensing region. For the planar electrode geometry in this work, sensitivity region tends to have a trapezoidal or semi-spherical shape in the vertical direction near the electrode surface [37, 38]. Consequently, the 3-D conductivity distribution near the substrate could be estimated based on the measured data. The sensitivity of the proposed sensor can be assessed by the row summation of the Jacobian matrix, which is formulated as:

$$J_{ij}(x,y,z) = -\int_{voxel\ \varkappa} \nabla u(I^i) \cdot \nabla u(I^j) d\mathcal{H} \qquad (16)$$

where $J_{ij}(x,y,z)$ denotes the sensitivity amplitude at voxel (x,y,z) when the electrode pair i is injected with current and the differential voltage on another pair j is measured. $u(I^i)$ and $u(I^j)$ denote respectively the induced electrical potential when the i^{th} and j^{th} pair of electrodes are injected with currents.

Fig. 7 shows the logarithmic sensitivity at the vertical cross section passing the electrodes 5, 6, 17, 14, 13 as highlighted by the red color. The result demonstrates that the amplitude of sensitivity decreases with the increase of layer indices, and due to the evenly distributed electrode layout in the circular sensing area, comparable sensitivity can be obtained with the increase of voxel indices. Overall, reasonable sensitivity values are obtained below layer 10 whilst the upper layers have smaller sensitivities.

Phantom simulations were performed in order to quantify the feasible depth of effective sensing region. Four spheroids with the same diameter of 1.5 mm were placed at various positions along the cross plane in Fig. 7. Fig. 8 presents the reconstructions of the phantoms by using Eq. (10) and Eq. (12), where the red circle indicates the true position of the spheroid. The results indicate that a) the horizontal positions of the spheroids can be well estimated, and b) the vertical positions of the spheroids below layer index 8 can be correctly calculated, and c) the spheroids at layer index 10 can be reconstructed but the vertical position is misplaced, and d) the spheroids higher than layer index 10 can hardly be reconstructed due to the small sensitivity in this region. Consequently, the 3-D image reconstruction can be effectively performed when the objects are located below layer index 10. Since the cell aggregates in this study sink at the bottom below layer index 6 of the sensing chamber, 3-D conductivity imaging is feasible.

IV. Results and Discussion

A. Cell Culture

Cell aggregate phantom experiments and dynamic cell-drug response experiment were performed by using the designed sensor and MCF-7 breast cancer cells in this section. The monolayer MCF-7 breast cancer cells were cultured routinely in a humidified 5% CO_2 incubator in 37 degrees Celsius. The culture medium was Dulbecco's Modified Eagle Medium: Nutrient Mixture F-12 (DMEM/F-12) supplemented with 10% fetal bovine serum (FBS) and 1% penicillin/streptomycin. The cells were trypsinized using 0.25% Trypsin for 3 minutes and counted under the microscope with the hemocytometer. Cell

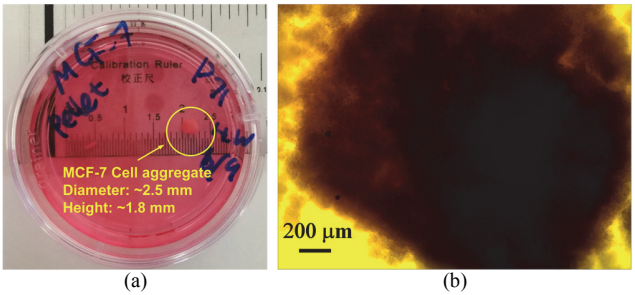

(a) (b)

Fig. 9. The MCF-7 cell spheroid to be imaged. (a) The picture of a MCF-7 cell spheroid (in yellow circle) within cell culture medium. (b) The microscope image of the cell spheroid.

suspension with 10 million cells was pipetted into a 15 ml conical tube and centrifuged at 1200 rpm for 5 minutes. The supernate was removed and the cells were cultured in the tube for one day with one milliliter fresh culture medium in order to form the spherical aggregate [39]. The cap of the tube was loosened to permit gas exchange.

Fig. 9 (a) shows the picture of the MCF-7 cell spheroid. The diameter of the spheroid was measured to be 2.5 mm and the height is measured to be 1.8 mm, leading to a diameter ratio of 20.83% and volume ratio of 1.26% with respect to the sensor. Fig. 9 (b) presents the microscope image of the cell spheroid captured by using the Olympus CK2 Inverted Microscope.

B. EIT System

The continuous, real-time impedance measurements were acquired based on the adjacent strategy [36] by using the multi-frequency EIT system [40] developed by the Agile Tomography Group, The University of Edinburgh. The picture of the system is shown in Fig. 10 (a). The system consists of 32 sensing electrodes and its working frequency ranges from 10 kHz up to 1 MHz. Arbitrary sensing strategy is attainable on the system. The highest SNR tested on a sensor with saline is 82.82 dB and the highest frame rate is 546 frames per second (fps) under serial mode and 1014 fps under semi-parallel mode. The system also includes a real-time 3-D imaging software named Visual Tomography [40], which is shown in Fig. 10 (b).

C. Cell Spheroid Phantom Imaging Results

The sensor's 3-D imaging performance was examined first on MCF-7 cell aggregate phantoms. Three different phantoms are presented in the first column of Fig. 11. In this test, the volume of cell culture medium was 700 microliters. According to the dimension of the sensor, the liquid level was calculated to be 6.2 mm. Therefore, the proportion of the cell spheroid in the vertical direction is around 29.03%, i.e. 5.8 layers of voxels.

3-D image reconstruction was performed based on the BPDN approach stated by Eq. (10) using the amplitude measurements. The algorithms parameters were the same as those stated in the paragraph below Eq. (10). The inversion was carried out by using Matlab 2014a installed on a desktop with an Intel Xeon X5650 CPU (2 processors @ 2.67 GHz) and 24 GB RAM.

Fig. 11 shows the 3-D image reconstruction results in the format of sliced images of each horizontal layer and synthetic

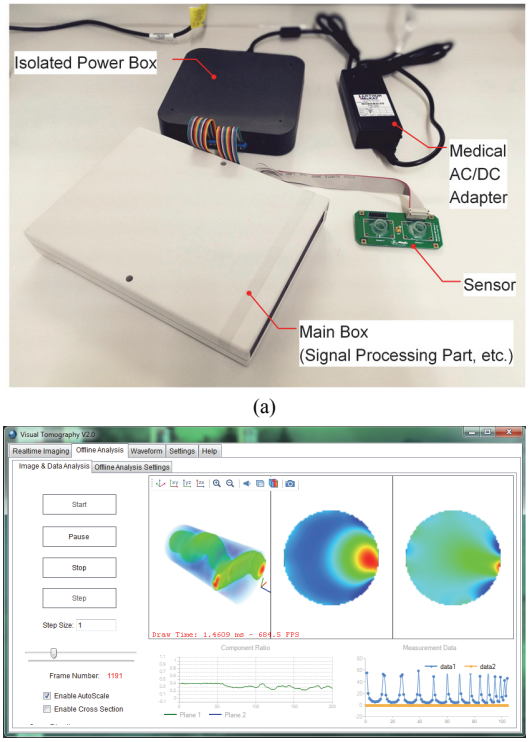

(a)

(b)

Fig. 10. The in-house developed multi-frequency EIT system. (a) Hardware. (b) 3-D imaging software: Visual Tomography.

3-D images. In this figure, the value of the colorbar indicates the relative change of conductivity with respect to the cell culture medium, which is a non-dimensional quantity. Table I presents the image reconstruction assessment results, including position error defined by Eq. (13), correlation coefficient defined by Eq. (14) and elapsed time of the algorithm.

The results suggest that: a) the local conductivity decreases, which are caused by the MCF-7 cell aggregates with various positions and numbers, could be correctly identified and imaged with small position errors (smaller than 0.08 mm) and large correlation coefficients (larger than 0.6400); b) the image quality is fairly good with few artefacts and spike noises; and c) the image reconstruction is time-efficient and all the computations were completed within 5 seconds.

D. Real-time Cell-drug Response Imaging Results

The real-time, continuous and non-destructive imaging of the dynamic interaction between the MCF-7 cell aggregate and diluted Triton X-100 solution was carried out by using the designed sensor in this subsection. The process of cell-drug response usually terminates in a few minutes [41]. For 3-D

TABLE I
IMAGE RECONSTRUCTION ASSESSMENT

Phantom	Position Error [mm]	Correlation Coefficient	Elapsed Time [s]
1	0.0492	0.6423	4.838
2	0.0778	0.7301	3.050
3	Left: 0.2857 Right: 0.0461	0.6445	2.864

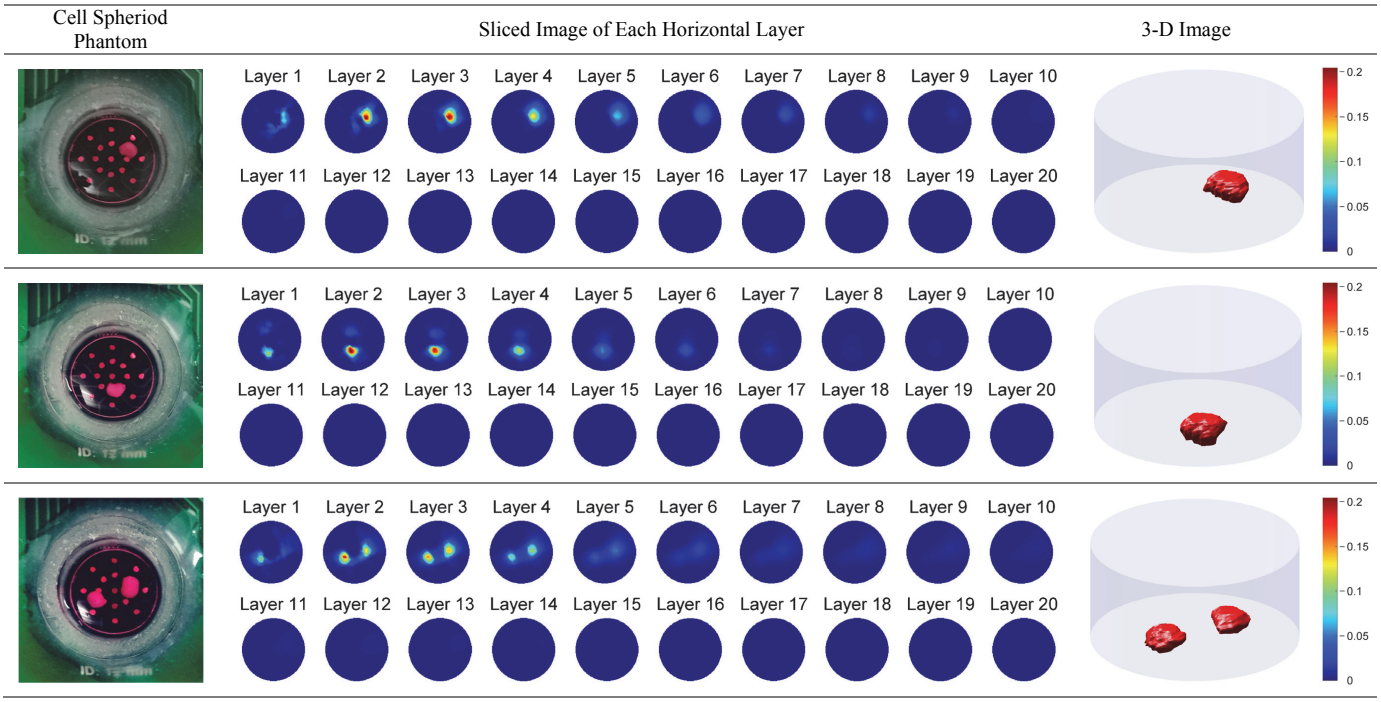

Fig. 11. 3-D image reconstructions of MCF-7 cell aggregate phantoms.

cultivated cell aggregates, this process cannot be visualized directly by optics based methods, such as microscopy, unless histological section is conducted. Therefore, a robust, fast and non-destructive method to screen such a transient process is demanded urgently for efficiency improvement and cost reduction of drug discovery.

In this test, Triton X-100 was utilized to lyse cells to permeabilize the membranes of MCF-7 cells. Consequently, the cancer cells would be killed [41]. Fig. 12 demonstrates the effect of Triton X-100 on MCF-7 cells. In order to examine cell status by the optical method, opaque cell solution, instead of cell aggregates, was adopted. Fig. 12 (a) and Fig. 12 (b) illustrate the cellular changes, captured 5 minutes after applying Triton X-100, from using 10×20 magnifications with the Olympus CK2 Inverted Microscope. The membranolysis and shrinkage of MCF-7 cells is observed clearly in the figure. Theoretically, the physiological status change of cells, caused by Triton X-100 or other similar drugs, can be indicated by conductivity variation indirectly [42]. This suggests that the proposed micro sensor is promising to visualize the process in 3-D.

Fig.13 illustrates the position of the MCF-7 cell aggregate in this experiment. The cell aggregate was placed near electrode 8

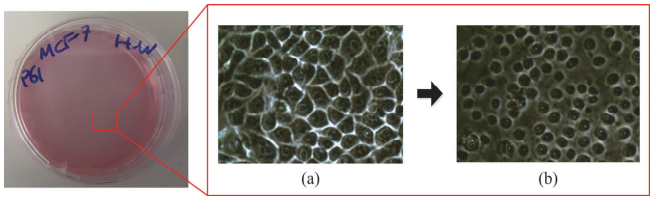

Fig. 12. Cellular changes captured by the microscope. (a) Before applying Triton X-100. (b) 5 minutes after applying Triton X-100.

and 10. Fig. 14 illustrates the experimental procedure for imaging the cell-drug response. Before the experiment began, the sensor was sterilized and, at time point t_0, 700 microliters of mixture of diluted Triton X-100 solution and cell culture medium was added to the sensing chamber. In this test, diluted Trion X-100 solution was pre-mixed with culture medium in concentration of 0.2%, which was achieved by adding 200 microliters 10% Triton X-100 solution in H_2O to 9.8 milliliters cell culture medium. The EIT system was then started to record measurements. After a few minutes of measuring the mixture, a MCF-7 cell spheroid was delivered at time point t_1, i.e. 319s.

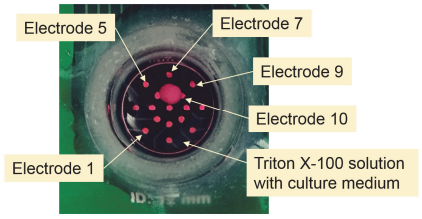

Fig. 13. Position of cell aggregate in cell-drug response test.

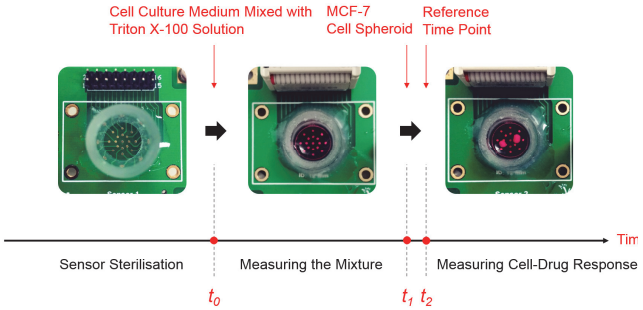

Fig. 14. The experiment procedure for imaging cell-drug response.

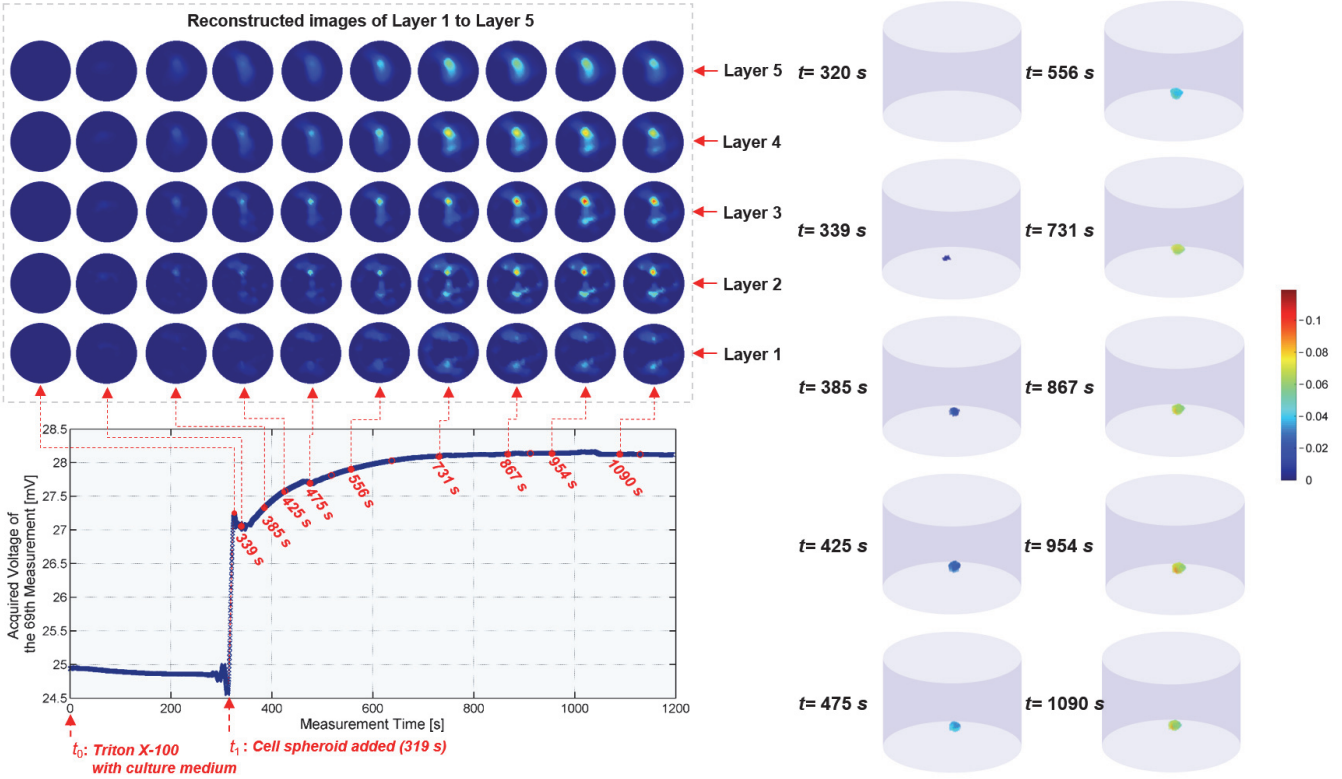

(a) (b)

Fig. 15. 3-D image reconstructions of cell-drug response. (a) Voltage response of the 69th measurement (electrode 7, 8 act as current injection, 9, 10 act as measurement) and sliced images from layer 1 to layer 5. (b) Synthetic 3-D images with respect to time.

According to previous studies, Triton X-100 can kill the cells in a few minutes [41]. Hence, the measuring process was terminated approximately 15 minutes later to ensure that the dynamic reaction was completely over.

3-D image reconstructions were conducted in time sequence to visualize the dynamic conductivity variation caused by the cell-drug response. In order to image the conductivity variation only associated with the drug effect, the measurement taken at one second after the cell addition, i.e. t_2=t_1+1 seconds (320s), was employed as a reference point to perform time-difference imaging. In addition, the time sequence of voltage response on the specific electrode pair, which was close to the position of the MCF-7 cell aggregate, was analyzed as well.

Fig. 15 (a) presents the time sequence of voltage response of the 69th measurement, in which the 7th and 8th electrodes were injected with currents while the differential voltage on the 9th and 10th electrodes was measured. The reconstructed images of layer 1 to layer 5 were also shown in a chronological order. The reason of only demonstrating the sliced images from layer 1 to layer 5 was that the conductivity variations were enriched in this region and nearly invisible in the other layers.

The measurement curve in Fig. 15 (a) suggests that the voltage change corresponding to each stage of the experiment procedure in Fig. 14 can be observed explicitly, including the measurement of the mixture between time point t_0 and t_1, the addition of the cell spheroid at time point t_1, and the cell-drug response process after time point t_1. Significant voltage variation was acquired after the cell spheroid was added to the mixture. This was associated directly with the cell-drug response process.

The sliced images from layer 1 to layer 5 in Fig. 15 (a) shows the trend of conductivity variation with respect to time which is able to correlate the measurement. Before 339 seconds, there is no significant conductivity variation; this indicates that the cell-drug response is still inadequate. However, from 385 seconds to 867 seconds, there appears a clear, continuous decline in conductivity within the area of the cell aggregate. This is because, after the cytomembrane is dissolved by Triton X-100, more and more cellular matrix, which is less conductive, enters the cell culture medium. From 867 seconds to 1090 seconds, a stationary stage is observed, where the conductivity variation nearly keeps the same. It indicates the end of the cell-drug response process.

Fig. 15 (b) shows the synthetic 3-D images of selected time points in Fig. 15 (a). In order to demonstrate the conductivity variation clearly, the conductivity value below 60% of the maximum value was set transparent in these 3-D images. The 3-D images correctly estimate the position of the cell-drug response and present the same conductivity changing trend with Fig. 15 (a).

The experiment study demonstrated that high quality 3-D tomographic images of the cell-drug response process were obtained by using the micro EIT sensor and the 3-D image reconstruction algorithm. By designing experiment procedure and selecting reference point carefully, these images demonstrate meaningful conductivity variations attributable to drug effect which could not be observed either visually or via optical methods such as a microscope.

E. Discussions

The MCF-7 cell aggregate phantoms experiments confirmed that the local conductivity contrast generated by the live cell aggregates could be reconstructed accurately by using the methods demonstrated in this work. The cell-drug response experiments further validated that real-time imaging of the conductivity changes in a transient process was feasible. Beyond that, the heating effects, influence of injected current, effect of contact impedance and potential challenges in long-term cell culture monitoring are also discussed as follows.

a) Heating effect. The heating effect in this work's sensing setup can be ignored according to the calculations based on the Joule-Lenz's law. The amplitude of injected alternating current was around 500 μA and the largest transimpedance was smaller than 20 ohm. Accordingly, the quantity of heat generated per second can be calculated as $Q_{max} = I_{rms}^2 Rt = (\frac{0.0005}{\sqrt{2}})^2 \times 20 \times 1 = 2.5 \times 10^{-6} J$. Considering the metallic ground plane beneath the sensing chamber, the infinitesimal heat can be dissipated rapidly.

b) Influence of injected current on cells. Continuous large current, e.g. 3 mA over 30 seconds, could wound the cell membranes [43]. The injected current in this work was carefully controlled (around 500 μA in amplitude) to avoid influence or destruction on cell membranes integrity. In addition, current injection to one electrode pair was controlled to less than 2 ms each time to avoid continuous current flow.

c) Influence of contact impedance. In absolute EIT image reconstruction, which estimates the absolute conductivity distribution, there can be a critical requirement for correct specification of contact impedance [44]. Whilst for difference imaging based on Eq. (7), which estimates the conductivity change with respect to a homogeneous background, the contact impedance is not as critical because it is commonly assumed that the contact impedance remains constant and that all measurement changes are due to internal conductivity changes. Therefore, the effect of contact impedance on image quality can be ignored in this work. Moreover, the contact impedance has been taken into account in the forward modelling process based on the method suggested in [45].

d) Effect of cell metabolism on cell culture medium. The electrical properties, such as the conductivity, of the cell culture medium may change slightly over time due to the exchange of ions and proteins between cells and medium. This is a critical issue that needs to be taken into account in the long-term cell culture process monitoring. In this study, the cell-drug response is a transient process which generally terminates in a few minutes. In such cases, the effect of cell metabolism on the medium conductivity can be ignored. In future work, to avoid the influence of cell metabolism on the medium conductivity in the long-term cell culture imaging, multi-frequency impedance tomography could be explored and frequency-difference rather than time-difference imaging method can be adopted, which is only relevant to the frequency responses of cells.

V. Conclusions

In this paper, we demonstrated a novel micro EIT sensor for real-time, non-destructive 3-D cultivated cell imaging. On the basis of the numerical analysis and experimental results, the following conclusions could be drawn.

- It is feasible to differentiate the low-conductive cell aggregates from the highly conductive cell culture medium using EIT by selecting proper current frequency based on the β-dispersion mechanism.
- The micro sensor provides the ability of visualizing the near-field 3-D conductivity distribution by using planar electrode configurations.
- High quality 3-D conductivity images were obtained in cell phantom experiments by using the 3-D image reconstruction algorithm. Beyond that, 3-D conductivity variation associated with the transient cell-drug response process was observed in real time, for the first time to the best of our knowledge.
- The proof-of-concept work demonstrated in this paper makes it possible to perform high quality 3-D cell imaging and real-time dynamic process monitoring within a 3-D cell culture system, which cannot be achieved by other imaging modalities to date. The high image quality guarantees, also, reliable and accurate quantitative analysis of the cell-drug response process and other studies of cellular dynamics.

Future work will extend the application of the sensor to image the 3-D cell culture process in long term and in the format of multi-frequency current injection.

References

[1] D. C. Barber and B. H. Brown, "Applied Potential Tomography," *Journal of Physics E-Scientific Instruments,* vol. 17, pp. 723-733, 1984.

[2] W. R. B. Lionheart, "EIT reconstruction algorithms: pitfalls, challenges and recent developments," *Physiological Measurement,* vol. 25, pp. 125-142, Feb 2004.

[3] R. H. Bayford, "Bioimpedance tomography (Electrical impedance tomography)," *Annual Review of Biomedical Engineering,* vol. 8, pp. 63-91, 2006.

[4] Y. Yang, J. Jia, N. Polydorides, and H. McCann, "Effect of structured packing on EIT image reconstruction," in *Imaging Systems and Techniques (IST), 2014 IEEE International Conference on*, 2014, pp. 53-58.

[5] Q. Wang, J. Polansky, B. Karki, M. Wang, K. Wei, C. H. Qiu*, et al.*, "Experimental tomographic methods for analysing flow dynamics of gas-oil-water flows in horizontal pipeline," *Journal of Hydrodynamics,* vol. 28, pp. 1018-1021, Dec 2016.

[6] O. P. Tossavainen, M. Vauhkonen, and V. Kolehmainen, "A three-dimensional shape estimation approach for tracking of phase interfaces in sedimentation processes using electrical impedance tomography," *Measurement Science and Technology,* vol. 18, pp. 1413-1424, May 2007.

[7] C. Carletti, G. Montante, C. De Blasio, and A. Paglianti, "Liquid mixing dynamics in slurry stirred tanks based on electrical resistance tomography," *Chemical Engineering Science,* vol. 152, pp. 478-487, Oct 2 2016.

[8] M. Hallaji, A. Seppanen, and M. Pour-Ghaz, "Electrical impedance tomography-based sensing skin for quantitative imaging of damage in concrete," *Smart Materials and Structures,* vol. 23, Aug 2014.

[9] D. Silvera-Tawil, D. Rye, M. Soleimani, and M. Velonaki, "Electrical Impedance Tomography for Artificial Sensitive Robotic Skin: A Review," *IEEE Sensors Journal,* vol. 15, pp. 2001-2016, Apr 2015.

[10] K. Y. Aristovich, B. C. Packham, H. Koo, G. S. dos Santos, A. McEvoy, and D. S. Holder, "Imaging fast electrical activity in the brain with electrical impedance tomography," *Neuroimage,* vol. 124, pp. 204-213, Jan 1 2016.

[11] E. K. Murphy, A. Mahara, and R. J. Halter, "Absolute Reconstructions Using Rotational Electrical Impedance Tomography for Breast Cancer

Imaging," *IEEE Transactions on Medical Imaging,* vol. 36, pp. 892-903, Apr 2017.
[12] B. Vogt, S. Pulletz, G. Elke, Z. Q. Zhao, P. Zabel, N. Weiler, *et al.*, "Spatial and temporal heterogeneity of regional lung ventilation determined by electrical impedance tomography during pulmonary function testing," *Journal of Applied Physiology,* vol. 113, pp. 1154-1161, Oct 2012.
[13] J. Yao, H. Obara, A. Sapkota, and M. Takei, "Development of three-dimensional integrated microchannel-electrode system to understand the particles' movement with electrokinetics," *Biomicrofluidics,* vol. 10, Mar 2016.
[14] M. Ravi, V. Paramesh, S. R. Kaviya, E. Anuradha, and F. D. P. Solomon, "3D Cell Culture Systems: Advantages and Applications," *Journal of Cellular Physiology,* vol. 230, pp. 16-26, Jan 2015.
[15] S. Breslin and L. O'Driscoll, "Three-dimensional cell culture: the missing link in drug discovery," *Drug Discovery Today,* vol. 18, pp. 240-249, Mar 2013.
[16] M. Vinci, S. Gowan, F. Boxall, L. Patterson, M. Zimmermann, W. Court, *et al.*, "Advances in establishment and analysis of three-dimensional tumor spheroid-based functional assays for target validation and drug evaluation," *Bmc Biology,* vol. 10, Mar 22 2012.
[17] E. A. Phelps, C. Cianciaruso, J. Santo-Domingo, M. Pasquier, G. Galliverti, L. Piemonti, *et al.*, "Advances in pancreatic islet monolayer culture on glass surfaces enable super-resolution microscopy and insights into beta cell ciliogenesis and proliferation (Vol 7, Pg 45961, 2017)," *Scientific Reports,* vol. 7, May 9 2017.
[18] E. Sarro, M. Lecina, A. Fontova, F. Godia, R. Bragos, and J. J. Cairo, "Real-time and on-line monitoring of morphological cell parameters using electrical impedance spectroscopy measurements," *Journal of Chemical Technology and Biotechnology,* vol. 91, pp. 1755-1762, Jun 2016.
[19] K. F. Lei, B.-Y. Lin, and N.-M. Tsang, "Real-time and label-free impedimetric analysis of the formation and drug testing of tumor spheroids formed via the liquid overlay technique," *RSC Advances,* vol. 7, pp. 13939-13946, 2017.
[20] F. Piccinini, A. Tesei, C. Arienti, and A. Bevilacqua, "Cell Counting and Viability Assessment of 2D and 3D Cell Cultures: Expected Reliability of the Trypan Blue Assay," *Biological Procedures Online,* vol. 19, p. 8, July 20 2017.
[21] C. Holmes, J. Daoud, P. O. Bagnaninchi, and M. Tabrizian, "Polyelectrolyte Multilayer Coating of 3D Scaffolds Enhances Tissue Growth and Gene Delivery: Non‐Invasive and Label‐Free Assessment," *Advanced healthcare materials,* vol. 3, pp. 572-580, 2014.
[22] K. S. Cheng, D. Isaacson, J. C. Newell, and D. G. Gisser, "Electrode Models for Electric-Current Computed-Tomography," *IEEE Transactions on Biomedical Engineering,* vol. 36, pp. 918-924, Sep 1989.
[23] E. Somersalo, M. Cheney, and D. Isaacson, "Existence and Uniqueness for Electrode Models for Electric-Current Computed-Tomography," *Siam Journal on Applied Mathematics,* vol. 52, pp. 1023-1040, Aug 1992.
[24] M. Vauhkonen, D. Vadasz, P. A. Karjalainen, E. Somersalo, and J. P. Kaipio, "Tikhonov regularization and prior information in electrical impedance tomography," *IEEE Transactions on Medical Imaging,* vol. 17, pp. 285-293, Apr 1998.
[25] L. H. Peng, H. Merkus, and B. Scarlett, "Using regularization methods for image reconstruction of electrical capacitance tomography," *Particle & Particle Systems Characterization,* vol. 17, pp. 96-104, Oct 2000.
[26] K. Heileman, J. Daoud, and M. Tabrizian, "Dielectric spectroscopy as a viable biosensing tool for cell and tissue characterization and analysis," *Biosensors & Bioelectronics,* vol. 49, pp. 348-359, Nov 15 2013.
[27] R. K. Rasel, C. Gunes, Q. M. Marashdeh, and F. L. Teixeira, "Exploiting the Maxwell-Wagner-Sillars Effect for Displacement-Current Phase Tomography of Two-Phase Flows," *IEEE Sensors Journal,* vol. 17, pp. 7317-7324, Nov 15 2017.
[28] R. K. Rasel, C. E. Zuccarelli, Q. M. Marashdeh, L. S. Fan, and F. L. Teixeira, "Toward Multiphase Flow Decomposition Based on Electrical Capacitance Tomography Sensors," *IEEE Sensors Journal,* vol. 17, pp. 8027-8036, Dec 15 2017.
[29] H. P. Schwan, "Mechanisms Responsible for Electrical-Properties of Tissues and Cell-Suspensions," *Medical Progress through Technology,* vol. 19, pp. 163-165, 1993.
[30] S. Grimnes and Ø. G. Martinsen, "Alpha-dispersion in human tissue," in *Journal of Physics: Conference Series*, 2010, p. 012073.
[31] Y. Xu, X. Xie, Y. Duan, L. Wang, Z. Cheng, and J. Cheng, "A review of impedance measurements of whole cells," *Biosensors and Bioelectronics,* vol. 77, pp. 824-836, 2016/03/15/ 2016.
[32] X. Yin, Y. Yang, J. Jia, and C. Tan, "3D image reconstruction on a miniature planar EIT sensor using sparsity with median filter," in *2017 IEEE SENSORS*, 2017, pp. 1-3.
[33] S. S. B. Chen, D. L. Donoho, and M. A. Saunders, "Atomic decomposition by basis pursuit," *Siam Review,* vol. 43, pp. 129-159, Mar 2001.
[34] E. van den Berg and M. P. Friedlander, "Probing the Pareto Frontier for Basis Pursuit Solutions," *Siam Journal on Scientific Computing,* vol. 31, pp. 890-912, 2008.
[35] M. S. Darus, S. N. Sulaiman, I. S. Isa, Z. Hussain, N. M. Tahir, and N. A. M. Isa, "Modified Hybrid Median Filter for Removal of Low Density Random-Valued Impulse Noise in Images," *2016 6th IEEE International Conference on Control System, Computing and Engineering (Iccsce),* pp. 528-533, 2016.
[36] B. Brown and A. Seagar, "The Sheffield data collection system," *Clinical Physics and Physiological Measurement,* vol. 8, p. 91, 1987.
[37] H. Y. Wei, C. H. Qiu, and M. Soleimani, "Evaluation of planar 3D electrical capacitance tomography: from single-plane to dual-plane configuration," *Measurement Science and Technology,* vol. 26, Jun 2015.
[38] X. H. Hu and W. Q. Yang, "Planar capacitive sensors - designs and applications," *Sensor Review,* vol. 30, pp. 24-39, 2010.
[39] L. M. Zhang, P. Q. Su, C. X. Xu, J. L. Yang, W. H. Yu, and D. S. Huang, "Chondrogenic differentiation of human mesenchymal stem cells: a comparison between micromass and pellet culture systems," *Biotechnology Letters,* vol. 32, pp. 1339-1346, Sep 2010.
[40] Y. J. Yang and J. B. Jia, "A multi-frequency electrical impedance tomography system for real-time 2D and 3D imaging," *Review of Scientific Instruments,* vol. 88, Aug 2017.
[41] D. Koley and A. J. Bard, "Triton X-100 concentration effects on membrane permeability of a single HeLa cell by scanning electrochemical microscopy (SECM)," *Proceedings of the National Academy of Sciences of the United States of America,* vol. 107, pp. 16783-16787, Sep 28 2010.
[42] P. O. Bagnaninchi and N. Drummond, "Real-time label-free monitoring of adipose-derived stem cell differentiation with electric cell-substrate impedance sensing," *Proceedings of the National Academy of Sciences of the United States of America,* vol. 108, pp. 6462-6467, Apr 19 2011.
[43] W. Gamal, S. Borooah, S. Smith, I. Underwood, V. Srsen, S. Chandran, *et al.*, "Real-time quantitative monitoring of hiPSC-based model of macular degeneration on Electric Cell-substrate Impedance Sensing microelectrodes," *Biosensors & Bioelectronics,* vol. 71, pp. 445-455, Sep 15 2015.
[44] V. Kolehmainen, M. Vauhkonen, P. A. Karjalainen, and J. P. Kaipio, "Assessment of errors in static electrical impedance tomography with adjacent and trigonometric current patterns," *Physiological Measurement,* vol. 18, pp. 289-303, Nov 1997.
[45] N. Polydorides and W. R. B. Lionheart, "A Matlab toolkit for three-dimensional electrical impedance tomography: a contribution to the Electrical Impedance and Diffuse Optical Reconstruction Software project," *Measurement Science and Technology,* vol. 13, pp. 1871-1883, Dec 2002.

Xipeng Yin was born in Harbin, China, in 1980. He received the B.Eng. master's degree and the Ph.D. degree in electrical and electronics engineering from Northwestern Polytechnical University, China, in 2003, 2006 and 2010 respectively. He was an assistant, a Lecturer, and an Associate Professor with the School of Electronics and Information, Northwestern Polytechnical University, China, in 2006, 2008, and 2014 respectively. He is a visiting scholar of the Agile Tomography Group, School of Engineering, University of Edinburgh, U.K. His current research interest includes electrical impedance tomography and electrical capacitance tomography for biomedical and industrial imaging.

Hancong Wu (S'16) is a PhD student with the Agile Tomography Group, School of Engineering, University of Edinburgh. He received his BEng Hons degree both in Electronics and Electrical Engineering at the University of Edinburgh and in Electronic and Information Engineering at South China University of Technology in 2015. His current research interest is focused on multi-frequency Electrical Impedance Tomography for biomedical and biological imaging.

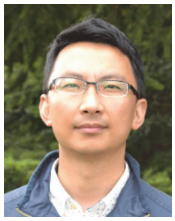

Jiabin Jia (M'15) was born in Inner Mongolia, China, in 1980. He received the B.Eng. and Master degree in Electrical and Electronics Engineering from the Wuhan University, China, in 2002 and 2005 respectively. After working for one year in H3C Technology Co., Ltd as a hardware engineer, he started his PhD study at the University of Leeds supported by the Overseas Research Students Award Scheme Award in 2006 and completed in 2010. Then he was a Research Fellow and worked on an EPSRC project for three years. In October 2013, he was appointed as a Lecturer in the School of Engineering, the University of Edinburg. His current research interests include electrical tomography, multiphase flow measurement, instruement development and medical imaging.

Yunjie Yang (M'13) received the B.Eng. (hons) and M.Sc. degrees in measurement & control engineering at Anhui University, China, in 2010, and Tsinghua University, China, in 2013, respectively. He completed his PhD study at the Agile Tomography Group, School of Engineering, University of Edinburgh, UK, in 2018. He is currently working as a Postdoc Research Associate in the same group. His current research interest includes bioimpedance tomography and chemical species tomography. He was the recipient of 2015 IEEE I&M Society Graduate Fellowship Award.